

## Research Article

# Compression Mechanical Properties and Constitutive Model for Soft–Hard Interlayered Rock Mass

Jinhua Li , Yang Yang , Pan Wang , Tianyu Zhang , Peili Su , and Songwei Zhao

*College of Architecture and Civil Engineering, Xi'an University of Science and Technology, Xi'an 710054, China*

Correspondence should be addressed to Yang Yang; [y\\_yang@stu.xust.edu.cn](mailto:y_yang@stu.xust.edu.cn)

Received 3 July 2023; Revised 12 March 2024; Accepted 28 March 2024; Published 12 April 2024

Academic Editor: Dingqiang FAN

Copyright © 2024 Jinhua Li et al. This is an open access article distributed under the Creative Commons Attribution License, which permits unrestricted use, distribution, and reproduction in any medium, provided the original work is properly cited.

The properties of soft–hard interbedded rock masses are significantly impacted by the strength of rock layers and the characteristics of interface surfaces. This study investigates the mechanical properties of soft–hard interlayered rock masses by preparing rock-like specimens with different interface angles. Uniaxial and triaxial compression tests were conducted to examine the compression mechanical characteristics of the specimens. Experimental results demonstrated that in the uniaxial compression tests, the peak strength of the two-layer rock-like specimen exhibits an initial decrease followed by an increase as the interface angle increases. Similarly, the peak strength of the three-layer rock-like specimen also follows a “U-shaped” pattern. The failure of both specimens shifts from tensile failure to shear failure. In the triaxial tests, the strength of the two-layer rock-like specimen initially increases and subsequently decreases as the interface angle increases. In contrast, the intensity of the three-layer rock-like specimen exhibits a decreasing trend, transitioning from shear dilation or tensile failure to shear failure. By utilizing the damage constitutive model to compute the compressive strength of the composite specimen, it was observed that the deviation from the experimental value did not exceed 2.5%, and the overall shape of the curves was in good agreement. Consequently, it is affirmed that the damage constitutive model developed in this study can accurately capture the pre-peak phase of the stress–strain relationship in soft–hard interlayered rock-like specimens, thus providing a valid representation of their mechanical behavior.

## 1. Introduction

Layered rock masses are widely distributed due to their long-term geological processes. Layered rock masses exhibit distinct mechanical properties compared to single rocks owing to the environmental conditions during their formation. These layered formations are characterized by heterogeneity and anisotropy. Current geotechnical engineering studies have focused on the mechanical properties of layered rock masses and their impact on construction, considering the challenges they pose for engineering projects such as underground space excavation, coal mining, and slope stability.

The physical and mechanical properties of a soft–hard combined rock mass can be visually determined by researchers through laboratory experiments. However, carefully selecting representative samples is crucial as they significantly influence the experimental outcomes. Stratified samples are meticulously chosen by scholars from the natural environment, and the orientations of natural joint surfaces are precisely determined.

Specimens are then acquired through drilling techniques to investigate the impacts of various dip angles, thickness ratios, and geometries on composite rock masses [1]. Due to the naturally deposited formation of rock samples, the distribution of joints and internal fractures is extremely random, posing significant difficulties in field sampling. Some scholars have proposed the use of adhesives and other materials to artificially create joint surfaces and bond layers of different properties into composite specimens [2]. This method allows for the free control of the position and shape of joint planes, yet it remains challenging to eliminate random fissures within the rock strata. Numerous scholars have resorted to similarity theory and proposed the utilization of quartz sand, river sand, and other aggregates, along with cement, kaolin, gypsum, and other binder materials, to fabricate rock-like specimens through the selection of appropriate material combinations [3, 4]. After verification, the prepared rock-analogous specimens effectively replicate the properties of the original rock. Consequently, this study employs these specimens to conduct subsequent research.

By conducting uniaxial compression experiments on rock samples with varying joint inclinations, scholars have observed a “U”-shaped variation curve in both peak stress and elastic modulus, which initially decreases and then increases with the increase in joint inclination. Moreover, the failure modes of the specimens under unidirectional loading exhibit distinct patterns: splitting failure perpendicular to the interface ( $0^{\circ}$ – $30^{\circ}$ ), shear sliding failure along the interface ( $45^{\circ}$ – $75^{\circ}$ ), and tensile failure along the interface ( $90^{\circ}$ ) [4–6]. To capture the failure processes of the specimens during loading, scholars have introduced an acoustic emission signal monitoring system and a DIC strain measurement device. These tools enable the acquisition of critical data such as crack development, deformation differences, and energy evolution in composite specimens with various joint inclinations under uniaxial loading. This information is subsequently utilized to analyze further the impact of joint inclination on the composite specimens [7–10]. With the advancement of numerical simulation software such as PFC, Wang et al. [11] and Chen et al. [12] have analyzed layered rock masses by incorporating numerical models to investigate the failure processes of specimens through the evolution of microcracks. Consistent with experimental observations, they also discovered that the strength of the specimens initially decreases and then increases with an increase in joint inclination. The failure location gradually shifts from the softer rock to the joint plane.

Due to the existence of joint planes, layered rock masses exhibit unique anisotropy. Based on the generalized Hooke’s law, Lekhnitskii derived the general equations of elastic theory for anisotropic materials, providing a theoretical foundation for addressing the anisotropy of materials [13]. Scholars have introduced parameters related to joint inclination angles into classical theories such as the Mohr–Coulomb strength theory, the Cosserat elastoplastic model, the Mises–Schleicher criterion, and the Hoek–Brown failure criterion. This integration aims to construct theoretical models that reflect the unique characteristics of composite rock masses [14–16]. Zhang and Liu [17] established the angular relationship  $\beta$  between the shear failure plane and bedding planes in layered rock masses. They investigated the variations of cohesion  $c$  and internal friction angle  $\varphi$  within the layered rock masses as a function of  $\beta$ . Based on these findings, they derived a theoretical model for the shear strength of layered rock masses. Huang et al. [18] separately considered the characteristics of individual rock layers and structural planes. By integrating the theory of transverse isotropy, they established constitutive relationships, yield criteria, and hardening–softening models for both the rock layers and structural planes. These models collectively represent the properties of layered rock masses. Some scholars have also defined parameters related to the thickness ratio between hard and soft rock strata, aspect ratio, and mechanical properties of rock strata through extensive experimental results. These parameters characterize the strength properties of specimens composed of alternating hard and soft rock layers [19–21]. After observing the failure modes of numerous specimens, Tien et al. [22] classified the ultimate failure modes of composite rock specimens into two

significant categories: sliding failure along discontinuity planes and non-sliding failure along discontinuity planes.

The deformation and failure of rocks are consequences of the accumulation of internal damage. By incorporating the theory of damage mechanics, a damage constitutive model for rocks was effectively established, reflecting the properties of composite rock masses consisting of alternating hard and soft layers. Scholars often defined damage based on the proportion of failed microelements. Statistical damage constitutive models were established by leveraging statistical laws, such as those of Weibull, and incorporating the assumption of strain equivalence [23–26]. Wang et al. [27] comprehensively considered the structural effects of rock masses and their coupling with loads, leading to the establishment of a damage evolution model and a damage constitutive model specifically for jointed rock masses. The patterns of damage evolution in layered rocks were reflected using acoustic emission counts by Fu et al. [28]. Ma et al. [29] established a 3D creep damage constitutive model in conjunction with the generalized Hoek–Brown model. Given the advantages and disadvantages of examining rock damage from different perspectives, this paper focused on developing a statistical damage constitutive model.

Current research on soft–hard interlayered rocks with different joint inclinations has yet to consider the influence of coupling effects between multiple joint planes on the properties of the specimens. Additionally, more studies must be done on the impact of the thickness ratio between soft and hard layers. Therefore, this paper focuses solely on studying soft–hard composite rock masses with one and two sets of joint planes. First, by combining ratio tests, specimens resembling soft–hard interlayered rocks were prepared using cement, gypsum, and quartz sand. Subsequently, nuclear magnetic resonance (NMR) technology was employed to inspect and screen the prepared specimens, ensuring their uniformity. Second, uniaxial and triaxial compression tests were conducted with an acoustic emission system to investigate the strength variation patterns and internal damage processes of soft–hard interlayered rocks under loading with different joint inclinations and combinations. Finally, a statistical damage constitutive model was constructed based on the experimental results.

## 2. Materials and Methods

### 2.1. Sample Preparation

*2.1.1. Select Proportioning Scheme.* Based on previous studies, this study employed M42.5 ordinary Portland cement and architectural gypsum as binding agents, with 100 and 200-mesh silica sand as aggregates to create rock-like specimens. A proportional experiment was designed (see Table 1). The uniaxial compressive strengths of the samples were determined to select the material ratios for soft and hard rocks in this study.

According to Protodyakonov’s Scale, the dividing line between soft rock and hard rock is determined by the firmness coefficient of  $f=2$ . Scheme 7 is designated for soft rock,

TABLE 1: Proportioning test design.

Group	Mass ratio of cement, gypsum, and silica sand	Water–cement ratio	Uniaxial compressive strength (MPa)
1	1:0.1:0.9	0.50	55.7
2	1:0.1:0.7	0.40	53.6
3	1:0.1:0.8	0.48	52.2
4	1:0.1:0.9	0.60	47.4
5	1:0.2:1	0.55	42.2
6	1:0.2:1	0.60	39.6
7	1:0.3:0.4	0.46	33.9
8	1:0.4:0.8	0.60	17.7
9	1:0.3:1.2	0.60	21.7
10	1:0.4:0.7	0.60	16.3

TABLE 2: Basic mechanical parameters of soft rock-like and hard rock-like.

Type of rock	Uniaxial compressive strength (MPa)	Elastic modulus (GPa)	Poisson	Cohesion (MPa)	Friction (°)
Hard rock-like	42.2	9.8	0.18	11.4	24.7
Soft rock-like	16.3	5.9	0.2	6.3	16.2

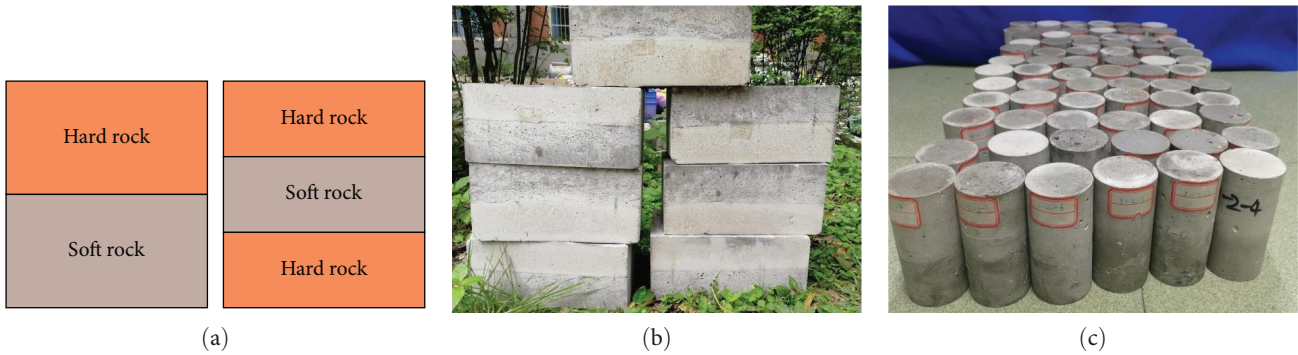


FIGURE 1: Placement scheme and specimens: (a) placement scheme; (b) pour specimens; (c) standard specimen.

exhibiting a firmness coefficient of  $f=1.6$ , which falls within Class VIa. The material composition for this scheme is as follows: “cement: 200-mesh silica sand: gypsum: water = 1 : 0.7 : 0.4 : 0.6.” Conversely, Scheme 8 pertains to Class V rock, characterized by a firmness coefficient of  $f=4.2$ . Therefore, the recommended material ratio for the preparation of hard rock is “cement: 100-mesh silica sand: gypsum: water = 1 : 1 : 0.2 : 0.55.”

The samples were designed using the selected material ratios for the soft and hard rock-like layers, and the corresponding mechanical parameters were measured (see Table 2).

**2.2. Prepare Composite Samples.** Samples of the soft–hard interlayered rock-like samples were prepared using two combinations: hard–soft (two-layer rock-like) and hard–soft–hard (three-layer rock-like) with corresponding thickness ratios of 1:1 and 1:1:1, respectively. The trial incorporated a layered pouring technique, which involves pouring soft rock-like after the hard rock-like has been poured and allowed to cure for 1 hr. This process enables a natural bond to form an interface between soft and hard rock-like. Carbon ink was added at the

early hard rock-like setting time to distinguish between the soft and hard rock-like layers (see Figure 1).

After a curing process of 28 days, the test samples were taken and processed into standard cylindrical test specimens with a diameter of 50 mm and a height of 100 mm. These specimens were then drilled at various angles ( $0^\circ$ ,  $10^\circ$ ,  $30^\circ$ ,  $45^\circ$ , and  $60^\circ$ ) to obtain specimens with different interface orientations. The specimens’ grouping schemes are presented in Table 3.

### 3. Sample Inspection

**3.1. Microscopic Inspection.** This study utilized NMR technology to screen the rock-like samples and reduce the influence of sample discreteness on the test results. By testing the nuclear magnetic signals generated by fluids in the samples, a transverse relaxation spectrum (T2 spectrum) was plotted. The area and porosity of the T2 spectrum were analyzed to select samples with few differences for subsequent tests. The average porosities of the samples are listed in Table 4.

The NMR processing method outlined in the “Determination of pore size distribution in coal and rock: nuclear

TABLE 3: Groups of the soft and hard rock-like specimens.

Placement scheme	Orientation of interface				
	0°	10°	30°	45°	60°
Hard–soft rock-like (two-layer rock-like)					
	(1-2)	(2-2)	(3-2)	(4-2)	(5-2)
Hard–soft–hard rock-like (three-layer rock-like)					
	(1-3)	(2-3)	(3-3)	(4-3)	(5-3)

TABLE 4: Average porosity of the samples.

Orientation of interface	Porosity of two-layer rock-like (%)	Porosity of three-layer rock-like (%)
0°	14.4	15.6
10°	11.7	13.7
30°	11.6	12.7
45°	10.8	14.5
60°	11.3	12.2

magnetic resonance method” (GB/T 42035-2022) was used to obtain a pore distribution diagram. Lutz et al. [30] divided rock pores into micropore (<1 μm), minipore (1–100 μm), mesopore (100–1,000 μm), and largepore (>1,000 μm).

Figure 2 shows the pore distribution diagrams of eight selected samples from a two-layer rock-like sample with an interface angle of 45°. Most of the pores in the samples were small, accounting for over 98% of the total porosity. To minimize the impact of sample discreteness on the test results, a rigorous sample selection was performed, and tests were conducted on samples with similar pore differences. Sample-5 and sample-6 were excluded from the analysis, while sample-1, sample-3, and sample-4 undergone the uniaxial compression tests, and sample-2, sample-7, and sample-8 were subjected to the triaxial compression tests.

The pore distributions of samples with different interface angles in the two-layer rock-like samples are presented in Figure 3. The samples exhibited a uniform distribution of pores, rendering them a reasonable approach for determining the mechanical properties of soft–hard interlayered rock-like samples with different combinations and interface angles.

3.2. Bond Strength of the Interface. In order to obtain the strength of the interface surface of the composite rock-like samples, we carried out the variable angle shear test and

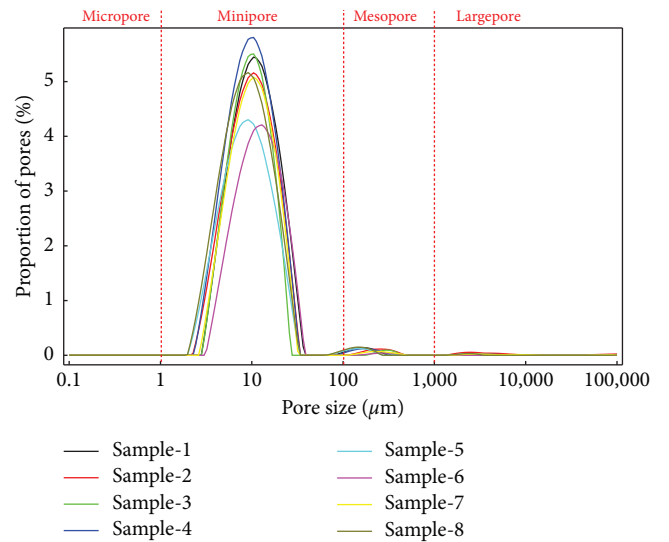


FIGURE 2: Pore distribution diagram of a two-layer rock-like sample with an interface angle of 45°.

measured the shear strength of the interface surface at 35°, 45°, and 55°. Finally, the cohesion of the interface surface is 1.806 MPa, and the internal friction angle is 42.61°. According to the *ISRM Suggested Method for Laboratory Determination*

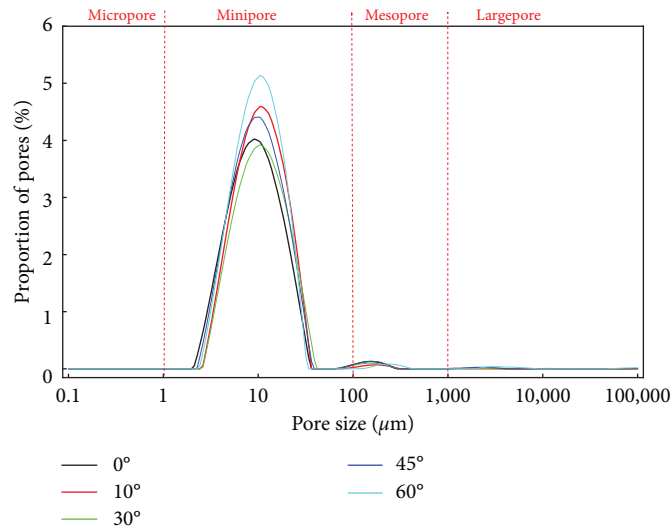


FIGURE 3: Pore distribution diagrams of two-layer rock-like samples with different interface angles.

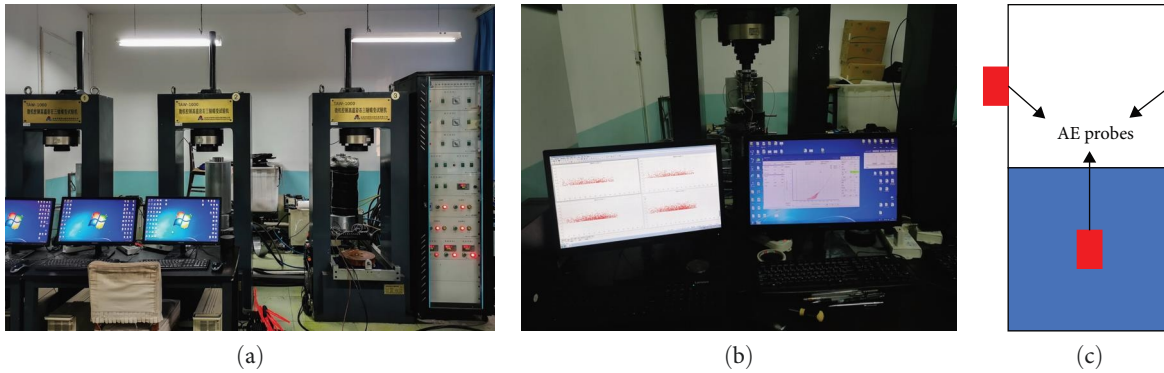


FIGURE 4: Testing equipment: (a) rock triaxial creep testing machine; (b) control system; (c) AE probes placement.

TABLE 5: AE system parameters.

Number of channels	Trigger mode	Threshold value	Pre-amplification (dB)	Sampling frequency (kHz)	Interface type	Conversion accuracy (bit)
4	Threshold triggering	40	40	30	USB3.0	16

of the Shear Strength of Rock Joints and the Engineering Rock Mass Classification Standard, the cohesion of the interface surface is greater than 0.22 MPa, and the internal friction angle is greater than  $37^\circ$ . It can be determined that the interface of the rock-like specimen is strong interface surfaces.

#### 4. Uniaxial (Triaxial) Test Procedure

**4.1. Testing Equipment.** The uniaxial and triaxial compression tests were conducted using a TAW-1000 microcomputer-controlled high-temperature rock triaxial creep testing machine. The built-in sensors of the machine were used to measure the axial and radial deformations of the specimens during the compression process (see Figure 4).

Additionally, a PAC AE generator was used to collect and record AE signals during the test, thereby monitoring the failure process of the specimens. The AE system parameters are shown in Table 5.

**4.2. Parameter Setting.** For the uniaxial compression test, a 0.05-mm/min loading rate was applied using a displacement control method once the device was entirely in contact with the specimen. Simultaneously, the PAC AE system collected AE signals. Loading was stopped when the specimen underwent significant damage or when the stress decreased to 50% of the peak stress.

The triaxial compression test adopted a confining pressure of 5 MPa and a loading rate of 0.05 mm/min. Loading

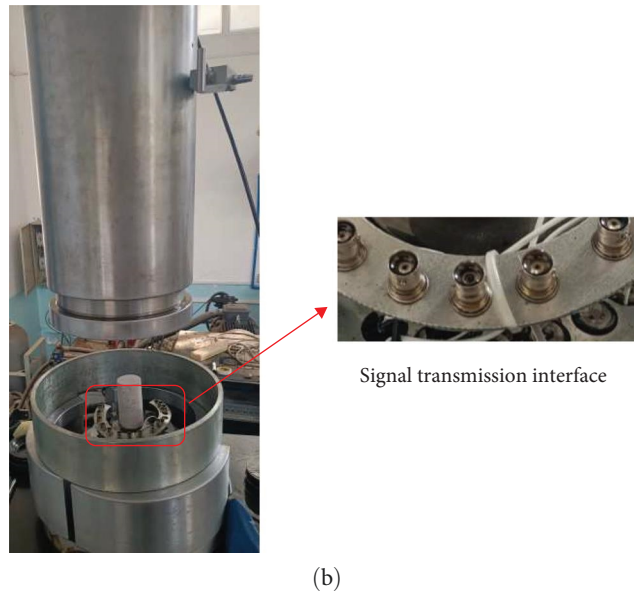
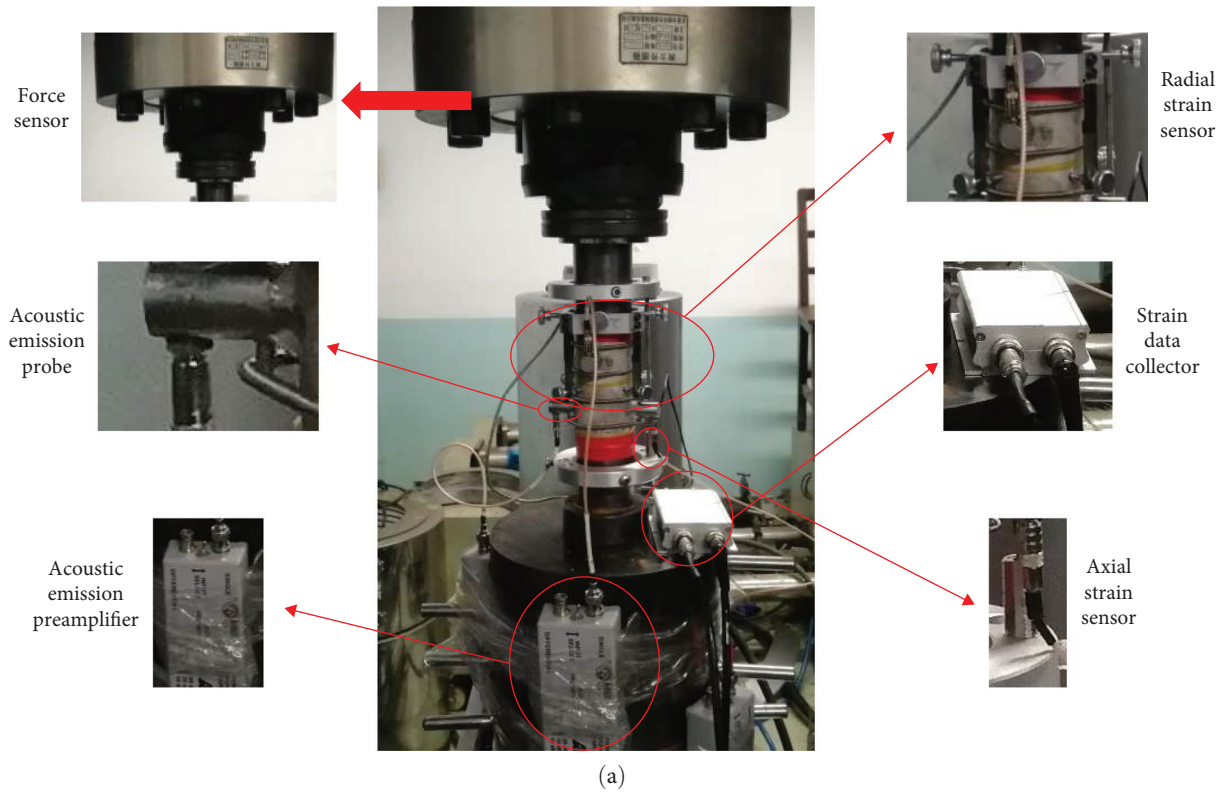


FIGURE 5: Test equipment: (a) uniaxial test; (b) triaxial test.

was stopped when the stress decreased to 50% of the peak stress.

4.3. Test Procedure

- (a) Cleaning up the workbench and loading platform and inspecting the equipment and instruments used.
- (b) Installing the specimen, attaching displacement sensors, and conducting axial and radial deformation tests.
- (c) Fixing AE probes and conducting AE signal detection, as shown in Figure 4(c) (due to spatial constraints, AE sensors are not set up in the triaxial test).
- (d) Putting the specimen on the level-loading platform and testing whether all the equipment functions properly (see Figure 5).

- (e) Entering the specimen dimensions and performing preloading.
- (f) To start the test, the uniaxial compression device button and the acoustic emission data save button are pressed.
- (g) Upon completion of loading, the sample is removed and cleaned from the workbench.

## 5. Compression Deformation Characteristics of Soft-Hard Interlayered Rock-Like

*5.1. Stress–Strain Characteristics of Uniaxial Compression Test Results.* The stress–strain curves and AE ringing rate–strain curves of the tested combined rock-like samples are shown in Figures 6 and 7, respectively.

Under unidirectional loading, the soft–hard interlayered rock-like specimens undergo four stages: initial compaction, elastic, elastic–plastic, and failure stages (see Figure 8).

- (a) Initial compaction stage. For rock-like samples with good densities, continuous compression occurs during initial loading, resulting in a reduction in porosity and further densification of the specimens. During this stage, the stress growth of the sample is not significant, but the change in strain is noticeable. As a result, the stress–strain curve often exhibits a concave shape. During the compaction stage, a few amounts of acoustic emission signals were generated due to the closure of initial cracks in the sample.
- (b) Elastic stage. During this stage, the stress applied to the sample increases linearly. Preexisting cracks in the sample continue to spread, resulting in the accumulation of a large amount of energy. However, the energy is still insufficient to overcome the constraints posed by internal agglomeration.
- (c) Elastic–plastic stage. The growth rate of the curve gradually slows until it reaches the peak stress, where the energy inside the sample is released, and the ringing count of the AE gradually increases. New cracks continue appearing inside the sample while existing cracks develop until the load-bearing capacity of the material is exceeded, resulting in sample failure.
- (d) Failure stage. After reaching the peak axial stress, the stress drops rapidly, and the ringing count of the AE increases sharply and reaches its peak. At this point, the energy accumulation inside the specimen exceeds the load-bearing capacity. A large amount of energy is instantly released, causing cracks to interconnect within the specimen and even leading to visible cracks on the surface of the specimen, ultimately leading to failure.

During the loading process of some rock-like samples, stress decreases after reaching the initial strength value and then increases upon further loading. This is because cracks are formed along the interface surface, but the properties of

the interface surface are partially recovered. After further loading, the cracks in the sample gradually close. The mutual constraint between the soft and hard layers still exists and has not yet reached the compressive strength limit of the soft–hard rock-like layers, resulting in an increase in the strength of the specimens. Until relative sliding occurs between the soft and hard layers and the resistance of the interface surface cannot withstand axial pressure, the specimen reaches the limit of compressive strength, and failure occurs. This process is often accompanied by the emergence of numerous new cracks, resulting in significant changes in AE counts.

The peak strength of a rock-like is a significant strength indicator that represents its load-bearing capacity (see Figure 9).

- (a) As the interface angle increases, the two-layer and three-layer rock-like samples exhibit significant variations in uniaxial compressive strength, which initially decreases and then increases. The strength decreases rapidly as the interface angle increases from  $0^\circ$  to  $30^\circ$ . When the interface angle is  $45^\circ$ , uniaxial compressive strength reaches its minimum value. However, the strength increased only slightly when the interface angle was  $60^\circ$ .
- (b) The peak strength of the three-layer rock-like samples is significantly higher than that of the two-layer rock-like samples, particularly in the interbedded rock-like samples with the interface angle of  $45^\circ$ , where the peak strength of the former exceeds that of the latter by more than two times.

The peak strain describes the deformation ability of rock-likes when they reach their peak strength (see Figure 10).

- (a) As shown in the graph, the range of the peak strain for the two-layer rock-like samples is between 0.3% and 0.8%, whereas that for the three-layer rock-like samples is between 0.48% and 0.68%. The peak strain of the three-layer rock-like samples shows more minor amplitude fluctuations than that of the two-layered rock-like samples, owing to a higher proportion of hard rock-like in the former rock-like block. This leads to a pronounced constraint effect on the soft rock-like.
- (b) In samples with small interface angles, failure primarily occurs within the internal soft rock-like layer, which possesses a relatively more substantial load-bearing capacity and significant compressive deformation, thus exhibiting a higher peak strain. When the sample fails along the interface surface, the interface surface undergoes shear slip deformation, whereas the individual rock-like layers produce a relatively small amount of compressive deformation. Therefore, the axial strain primarily depends on the shear slip deformation of the interface surface, resulting in a minor peak strain.

By analyzing the stress and strain of rock-likes during the elastic stage under loading, their elastic modulus can be

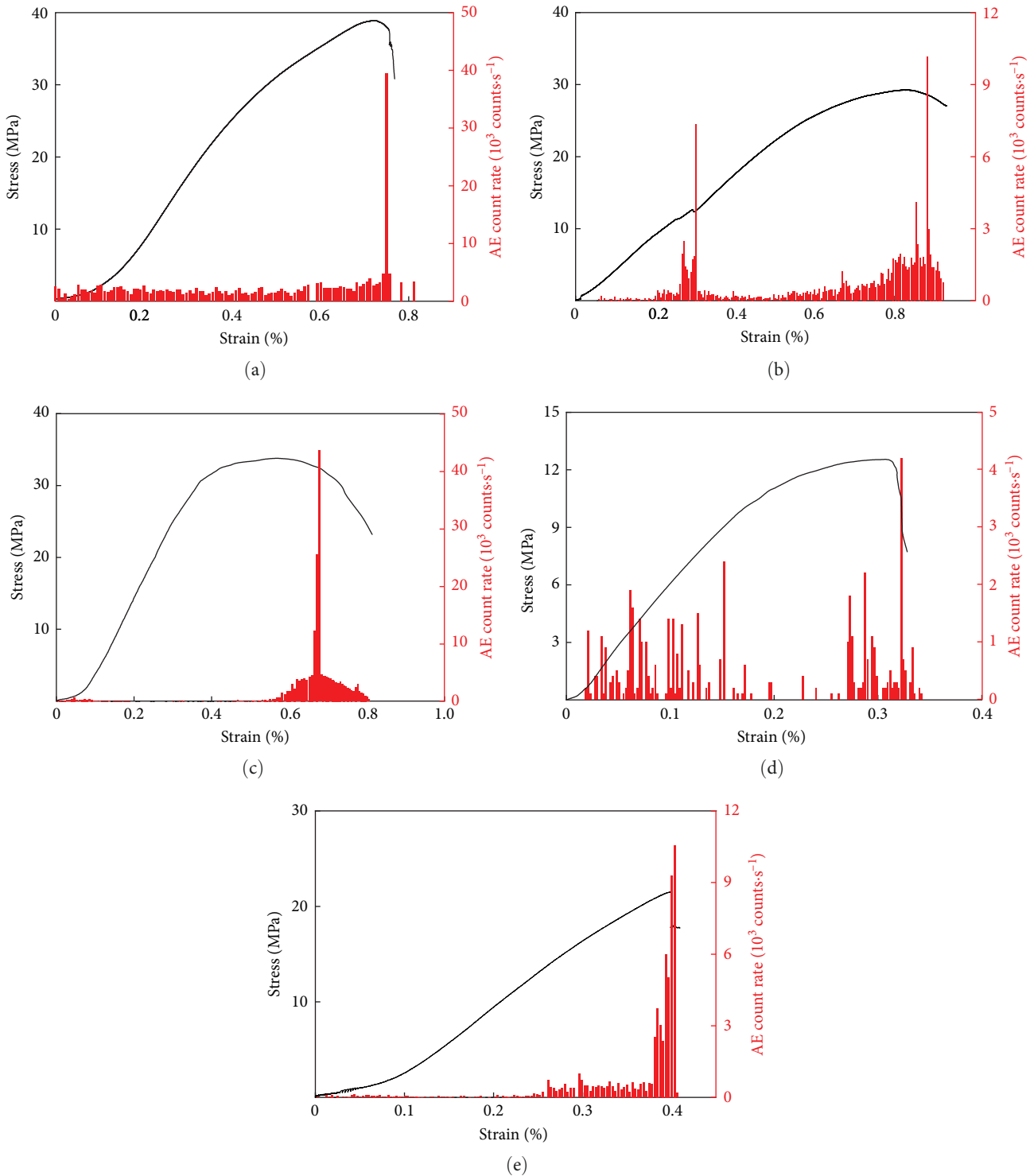


FIGURE 6: Stress–strain curves of the two-layer rock-like samples with different interface angles: (a) 0°; (b) 10°; (c) 20°; (d) 45°; (e) 60°.

obtained, which serves as an indicator of their deformation properties (see Figure 11).

The elastic modulus of the two-layer rock-like samples ranges from 5.2 to 7.5 GPa, which is between the elastic moduli of soft and hard rock-likes but close to that of soft rock-likes. The elastic modulus of the three-layer rock-like

samples is slightly higher than that of the two-layer rock-like samples, ranging from 8.7 to 14.2 GPa.

*5.2. Stress-Strain Characteristics of Triaxial Compression Test Results.* The typical stress–strain curves of the interbedded rock-like samples with varying interface angles using two



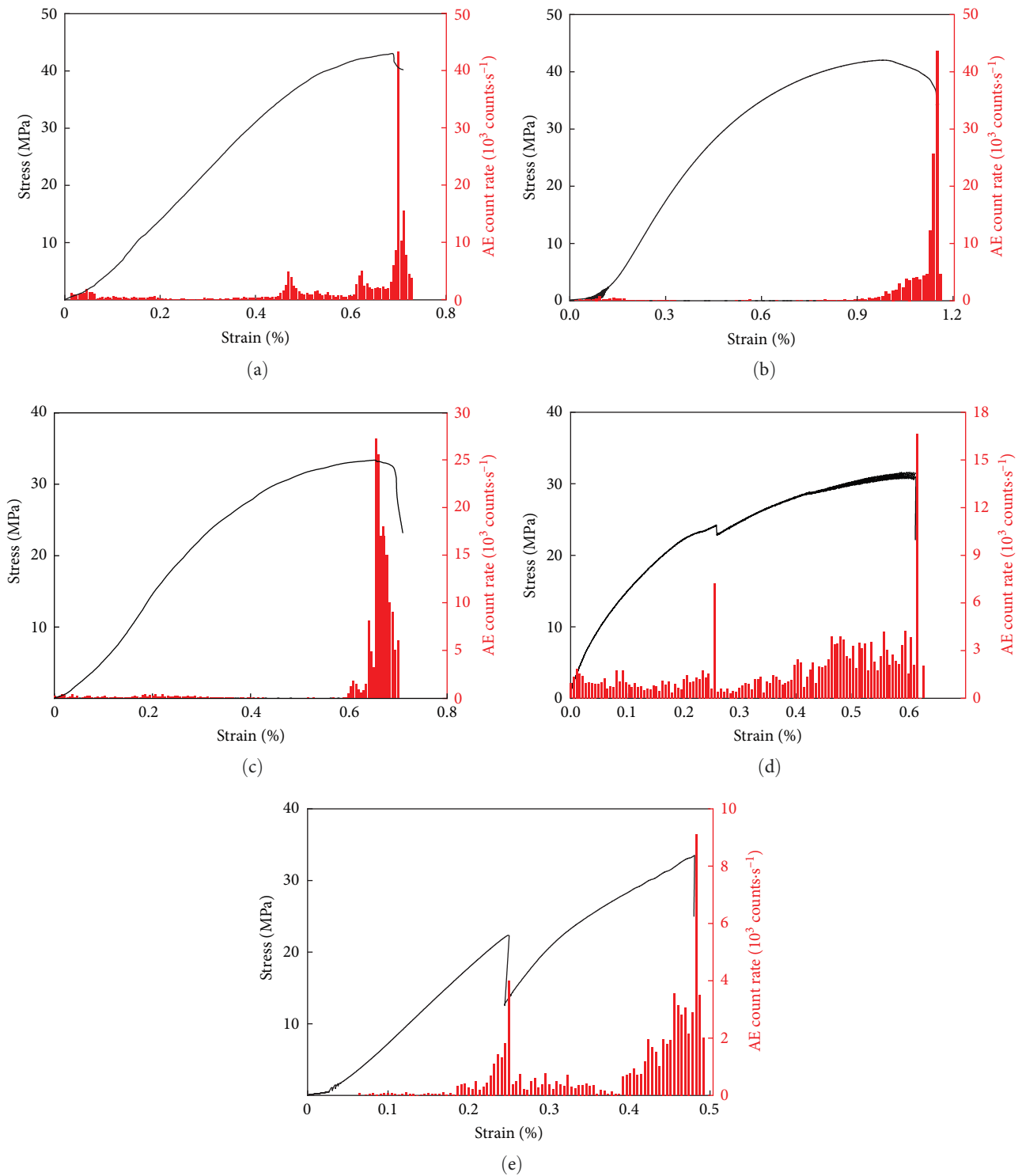


FIGURE 7: Stress–strain curves of the three-layer rock-like samples with different interface angles: (a) 0°; (b) 10°; (c) 20°; (d) 45°; (e) 60°.

combinations of hard and soft rock-like layers are shown in Figure 12.

(a) Compared to the stress–strain curve of the samples under uniaxial compression testing, the stress–strain curve of those under triaxial compression testing did not have a pronounced densification stage, as the

confining pressure was applied before axial loading. The sample underwent an elastic stage in the initial loading period, a plastic stage in the mid-loading period, and a failure stage in the later loading period. (b) During the elastic stage, the stress–strain curve of the samples in triaxial compression testing exhibited a faster linear growth rate than those in uniaxial compression.

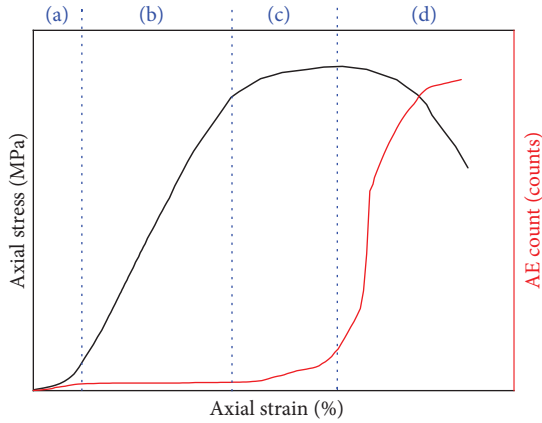


FIGURE 8: Stress–strain curve and AE count–strain curve of the sample. (a) Initial compaction stage. (b) Elastic stage. (c) Elastic–plastic stage. (d) Failure stage.

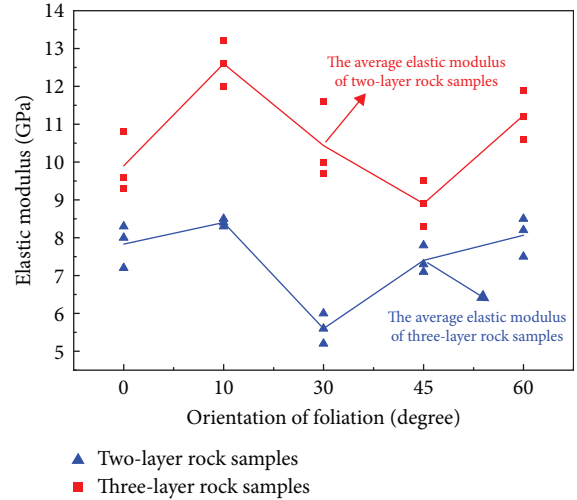


FIGURE 11: Elastic modulus under the uniaxial compression test.

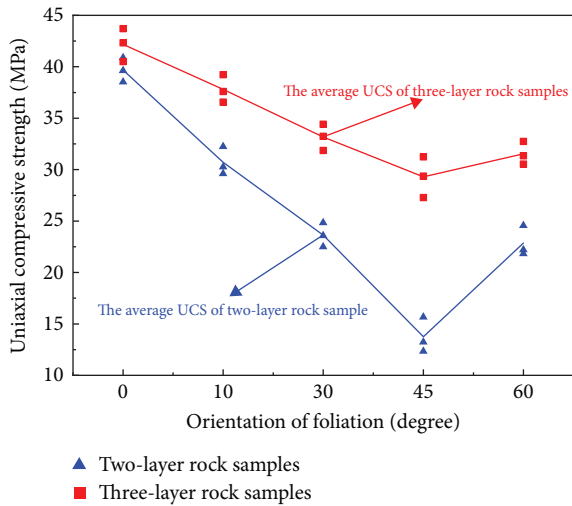


FIGURE 9: Peak strength under the uniaxial compression test.

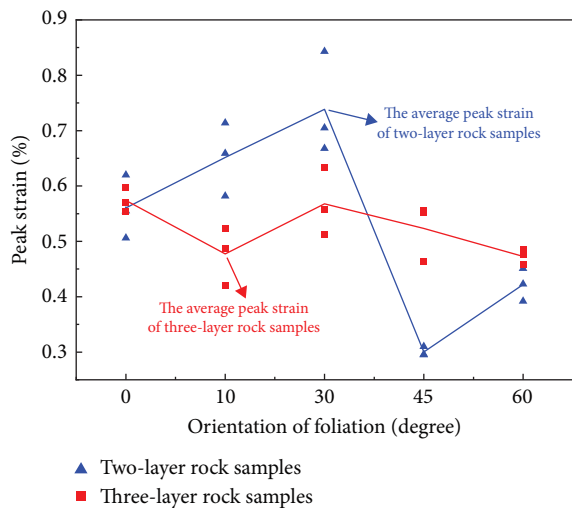


FIGURE 10: Peak strain under the uniaxial compression test.

(c) When the samples were in the failure stage, owing to the presence of a 5-MPa confining pressure, the ductile failure of the rock-like after the peak stress was apparent, and the samples exhibited a more significant yield plateau after the peak stress. When the interface orientation was between 0° and 30°, the yield plateau of the samples exhibited stress softening and ideal plasticity. When the interface orientation was 45° or 60°, the failure of the rock-like samples primarily manifested as a brittle failure, and the curve decreased rapidly after the stress reached the peak strength.

The stress state of rock-likes under confining pressure should be investigated as it is realistic to work conditions (see Figure 13).

- (a) For the two-layer rock-like samples, the peak strength first increased and then decreased as the interface orientation increased, reaching a maximum of approximately 50 MPa at an interface orientation of 45°. The rock-like samples combined with horizontal interfaces exhibited the lowest strength of 39 MPa. For the three-layer rock-like samples, the peak strength decreased as the interface orientation increased. The strength was the highest at an orientation of 0° and close to the uniaxial compressive strength of hard rock-like.
- (b) For interlayered rock-like samples with the same interface orientation, the strength of the three-layer rock-like samples with a more significant proportion of hard rock-likes was generally greater than that of the two-layer rock-like samples. Furthermore, the degree of enhancement was greater for specimens with horizontal interface surfaces.

By considering the strain values corresponding to the peak stresses of the specimens as the peak strain values (see Figure 14).

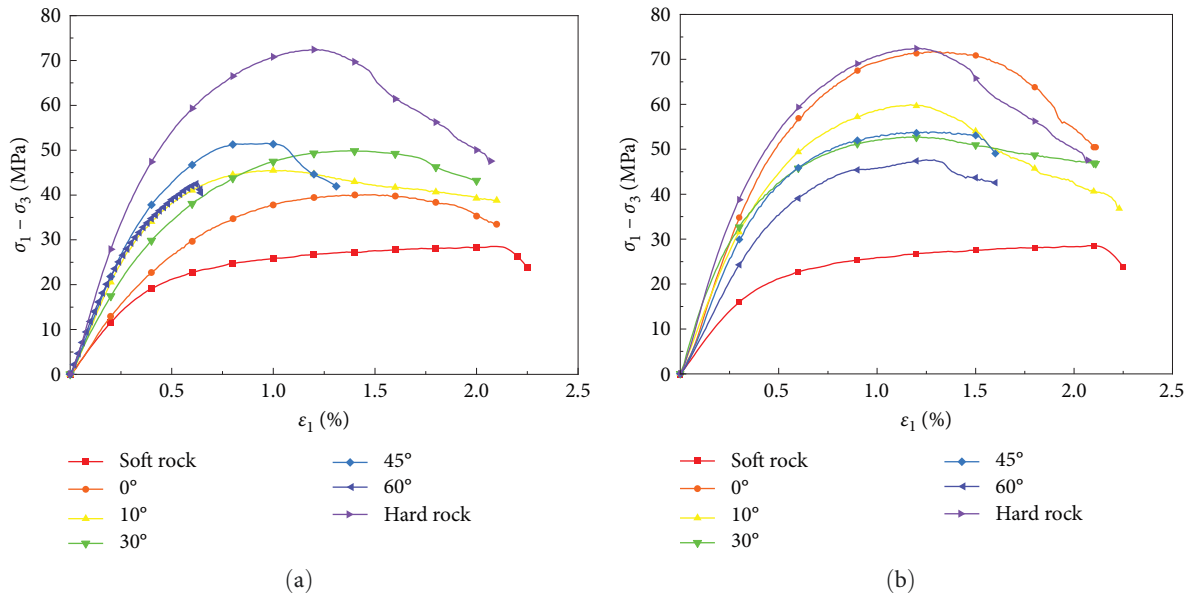


FIGURE 12: Stress–strain curve of samples under the triaxial test: (a) two-layer rock-like; (b) three-layer rock-like.

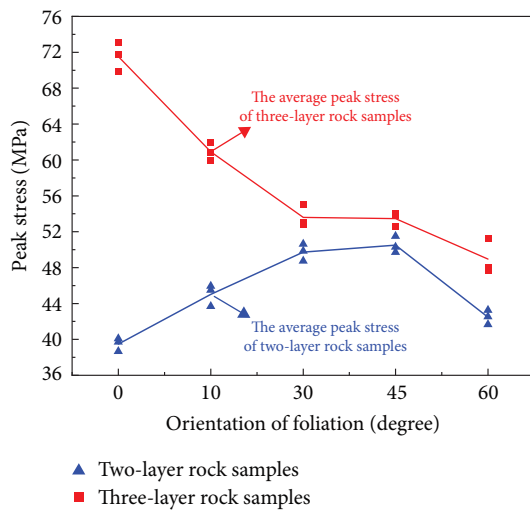


FIGURE 13: Peak strength under triaxial compression test.

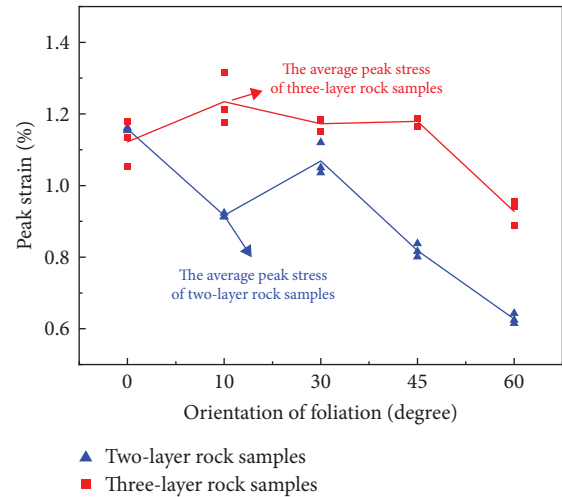


FIGURE 14: Peak strain under triaxial compression test.


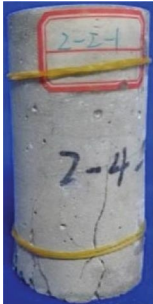



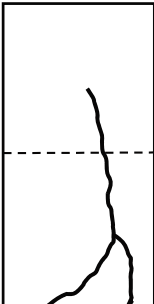
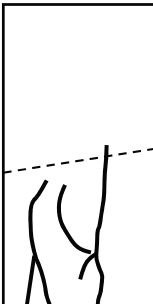
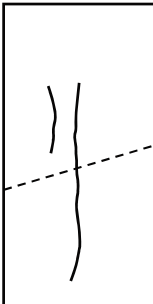
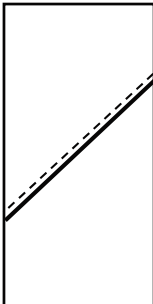

- (a) For the two-layer rock-like samples, the average strain value exhibited an increasing trend and then gradually decreased as the orientation of the interface increased. For the three-layer rock-like samples, the peak strain exhibits an “M” shape with an increase at 10° and 45°. Under triaxial loading, the axial deformation capacity of the soft–hard interlayered rock-like samples gradually weakened as the interface orientation increased.
- (b) The peak strain values of the three-layer rock-like samples were slightly higher than those of the two-layer rock-like samples. This indicates that hard rock-likes improve the ability of the specimens to resist axial deformation and enhance the deformation performance of the interlayered rock-like samples.

## 6. Failure Characteristics of Soft–Hard Interbedded Rock-Like

6.1. Failure Mode under Uniaxial Loading Conditions. Owing to the heterogeneity of the layered rock-like samples with varying hardness levels and the impact of interface surfaces, different combinations display diverse failure modes. The primary failure modes of the specimens can be classified into tensile splitting and shear sliding failures (see Tables 6 and 7).






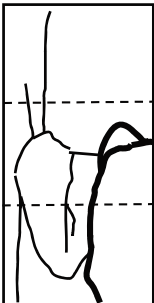
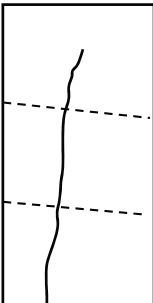


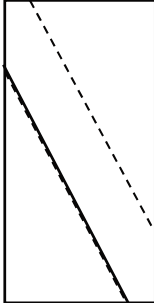
- (a) Tensile splitting failure. When the interface orientation was 0°, 10°, or 30°, numerous vertical cracks first appeared in the soft-rock-layer, resulting in severe damage on the surface. Then, these cracks propagated toward the hard-rock-layer and penetrated the specimen.

TABLE 6: Failure of two-layer rock-like samples under uniaxial compression test.

Orientation of interface	0°	10°	30°	45°	60°
Damage diagram					
Schematic diagram					

Note. Thickness of the line represents crack size.

TABLE 7: Failure of three-layer rock-like samples under uniaxial compression test.






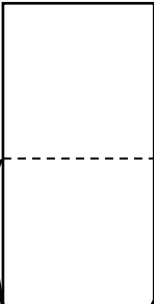
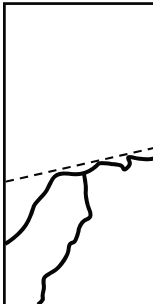
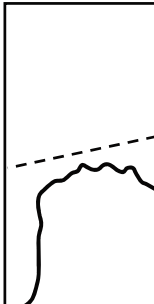
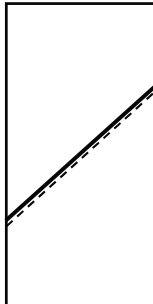
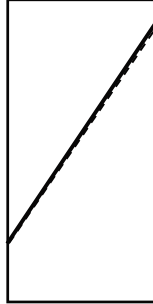
Orientation of interface	0°	10°	30°	45°	60°
Damage diagram					
Schematic diagram					

Note. Thickness of the line represents crack size.

(b) Shear sliding failure: When the interface orientation was 45° or 60°, the failure of the specimens primarily occurred on the interface surface, and cracks developed along the interface surface until failure. No significant damage within the soft-rock-layer and hard-






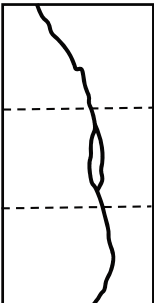
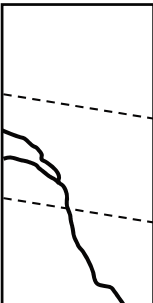
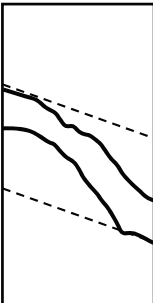
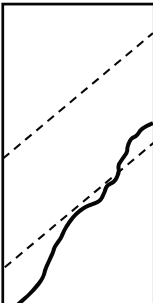
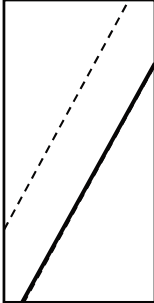
rock-layer was observed, indicating that the interface surface became the weak plane of the combined rock-like samples when the interface was relatively large, and the strength of the rock-layers was not fully utilized.

TABLE 8: Failure of two-layer rock-like specimen under triaxial compression test.

Orientation of interface	0°	10°	30°	45°	60°
Damage diagram					
Schematic diagram					

Note. Thickness of the line represents crack size.

TABLE 9: Failure of three-layer rock-like specimen under triaxial compression test.

Orientation of interface	0°	10°	30°	45°	60°
Damage diagram					
Schematic diagram					

Note. Thickness of the line represents crack size.

6.2. Failure Mode under Triaxial Loading Conditions. The failure modes of the soft–hard interlayered rock-like specimen during the triaxial compression tests are listed in Tables 8 and 9.

At an interface orientation of 0°, the lower part of the soft rock-like layer underwent shear dilation failure, whereas no significant damage occurred to the hard rock-like part of the two-layer rock-like samples. At interface orientation of 10°,

the failure of the two-layer rock-like samples was primarily due to several inclined and vertical cracks in the soft rock-like section. The failure of the two-layer rock-like samples occurred along the interface surface and extended to the inside of the soft rock-like when the interface orientation was 30°. For interface orientations of 45° and 60°, the two-layer rock-like samples experienced shear failure along the interface surface.

At an interface orientation of 0°, a crack penetrated the entire specimen in the three-layer rock-like samples, which differed from the shear dilation failure observed in the soft rock-like layer of the two-layer rock-like samples. At interface orientation of 10°, the failure of the three-layer rock-like samples was primarily attributed to a crack in the middle of the soft rock-like section and the lower part of the hard rock-like section, as well as a crack along the interface surface in the soft rock-like section. When the interface orientation was 30°, the first type of failure in the three-layer rock-like samples primarily occurred through two parallel cracks inside the middle soft rock-like layer along the interface surface. The second type of failure occurred as cracks opened along the interface surface and extended to the hard rock-like section. For an interface angle of 45°, the failure of the three-layer rock-like samples was primarily due to shear failure along the interface surface. At interface orientation of 60°, the failure of the three-layer rock-like samples was primarily caused by shear sliding failure along the interface surface, and no noticeable cracks were formed in the hard and soft rock-like layers.

Compared with the uniaxial compression tests, the confining pressure can lead to shear dilation failure in soft rock-like layers, consequently reducing the number of surface cracks on the specimens. When the interface angle falls within the range of 0°–30°, a significant difference in the failure mode of the specimen was observed. Notably, the failure mode no longer primarily undergoes tensile splitting but is characterized by shear failure. When the interface angle reached 45°–60°, the failure mode of the specimen was still characterized by shear failure along the interface surface, which became the weakest part of the specimen.

## 7. Damage Constitutive Model of Soft–Hard Interbedded Rock-Like

Based on the failure mode and AE characteristics of the rock-like samples under compression tests, the macroscopic failure of the rock-likes primarily originated from the extension of one or several prominent internal cracks. Therefore, we establish a damage constitutive model based on the statistical strength theory to characterize the failure behavior of the rock-like.

Considering the influence of interface surfaces on the performance of the soft–hard interlayered rock-like samples and based on related studies, the failure process of a rock-like is continuous. The following assumptions were made: (1) the soft–hard interlayered rock-like samples were a transversely isotropic material; (2) the contact between layers was tight, the interface surfaces were relatively smooth, and their

TABLE 10:  $m$  under uniaxial compression test.

Orientation of interface	0°	10°	30°	45°	60°
Two-layer rock-like	2.28	4.96	2.86	1.67	3.36
Three-layer rock-like	3.57	1.40	1.70	1.48	2.34

thickness was negligible; the normal deformation of the interface surfaces during loading must be addressed; and (3) stress in the rock-like samples is continuous.

*7.1. Establishment of Damage Constitutive Model.* According to the strain equivalence principle, the damage constitutive relationship of a rock under triaxial stress can be expressed as follows:

$$\sigma_1 = E\varepsilon(1 - D) + 2\nu\sigma_3, \quad (1)$$

where  $\sigma_1$  is the major principal stress,  $\sigma_3$  is the confining pressure,  $\varepsilon$  is the major principal strain,  $D$  is the damage variable,  $E$  is the elastic modulus, and  $\nu$  is Poisson's ratio.

Assuming that the failure of rock microelements follows the Weibull statistical law, the probability density function can be expressed as follows:

$$\varphi(\varepsilon) = \frac{m}{\varepsilon_0} \left(\frac{\varepsilon}{\varepsilon_0}\right)^{m-1} e^{-\left(\frac{\varepsilon}{\varepsilon_0}\right)^m}, \quad (2)$$

where  $m$  is the shape parameter of the Weibull distribution, and  $\varepsilon_0$  is the strain of the rock microelement.

Damage to rock materials is related to internal defects, which affect the strength of microelements and random failure. The relationship between the damage variable  $D$  and the density of the statistical distribution of microelement failure can be expressed as follows:

$$dD/d\varepsilon = \varphi(\varepsilon). \quad (3)$$

The deformation and failure of rocks under loading result from continuous damage and the failure of microelements in the rock, which is a continuous process. Therefore,  $D$  corresponds to the probability of the strength of microelements. Based on this relationship, the damage variable of the rock during loading can be obtained as follows:

$$D = \int_0^\varepsilon \varphi(\varepsilon) d\varepsilon = 1 - e^{-\left(\frac{\varepsilon}{\varepsilon_0}\right)^m}. \quad (4)$$

Based on the primary mechanical parameters of the stress–strain curve of rock during loading, the damage evolution equation is determined and combined with the constitutive relationship of rock; the statistical damage constitutive model of rock can be derived as follows:

$$\sigma_1 = E\varepsilon \exp\left[-\left(\frac{\varepsilon}{\varepsilon_0}\right)^m\right] + 2\nu\sigma_3. \quad (5)$$

*7.2. Determination of Model Parameters.* The parameters  $m$  and  $\varepsilon_0$  are closely related to the peak strength point of

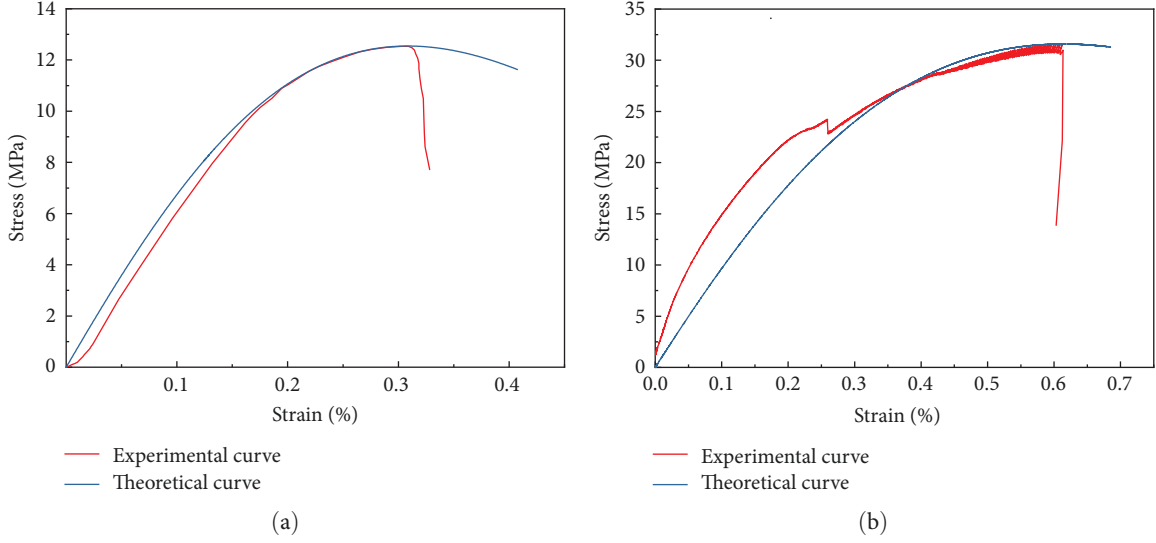


FIGURE 15: Comparison of experimental and theoretical results under uniaxial compression test: (a) two-layer rock-like with an interface orientation of 45°; (b) three-layer rock-like with an interface orientation of 45°.

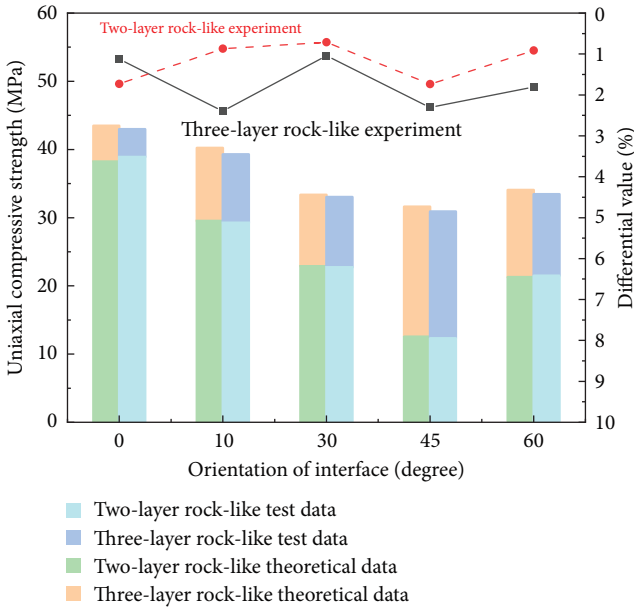


FIGURE 16: Difference between theoretical and experimental values of uniaxial compressive strength.

TABLE 11:  $m$  under triaxial compression test.

	0°	10°	30°	45°	60°
Two-layer rock-like	2.28	1.61	2.19	2.61	3.57
Three-layer rock-like	2.24	1.64	1.63	1.55	1.53

the stress–strain curve. Calculating the first derivative of Equation (5) with respect to  $\varepsilon$  yields:

$$d\sigma/d\varepsilon = E \exp \left[ -\left( \frac{\varepsilon}{\varepsilon_0} \right)^m \right] \left[ 1 - \left( \frac{\varepsilon}{\varepsilon_0} \right)^m \right], \quad (6)$$

$$\frac{\sigma_f}{E\varepsilon_f} = \exp \left[ -\left( \frac{\varepsilon}{a} \right)^m \right], \quad (7)$$

$$m = 1/\ln(E\varepsilon_f/\sigma_f). \quad (8)$$

We adopt  $\varepsilon_f$  as a model parameter for the parameter  $\varepsilon_0$ .

7.3. Model Verification under Uniaxial Compression Test. Under uniaxial loading, the confining pressure is 0; therefore, Equation (5) can be simplified to the following:

$$\sigma_1 = E\varepsilon \exp \left[ -\left( \frac{\varepsilon}{\varepsilon_0} \right)^m \right]. \quad (9)$$

Using Equation (8),  $m$  can be obtained (see Table 10).

The elastic modulus  $E$ , peak stress  $\sigma_f$ , and peak strain  $\varepsilon_f$  corresponding to the peak stress are obtained from the stress–strain curve of the uniaxial compression test. These mechanical parameters are required for the damage constitutive equations.

The experimental and theoretical curves for the sample with an interface angle of 45° are shown in Figure 15.

The triaxial compressive strength of two-layer rock mass and three-layer rock mass under different interface orientations were compared with the calculation results of the damage model (see Figure 16).

Results show that the proposed model can accurately describe the experimental results of the pre-peak stage of the stress–strain curve and that the parameters used have precise physical meanings, rendering the solution of the damage model relatively simple. However, this model has certain limitations. It could not accurately simulate the compaction stage of the curve during the test process, and because of the brittle failure of the rock-like, the damage

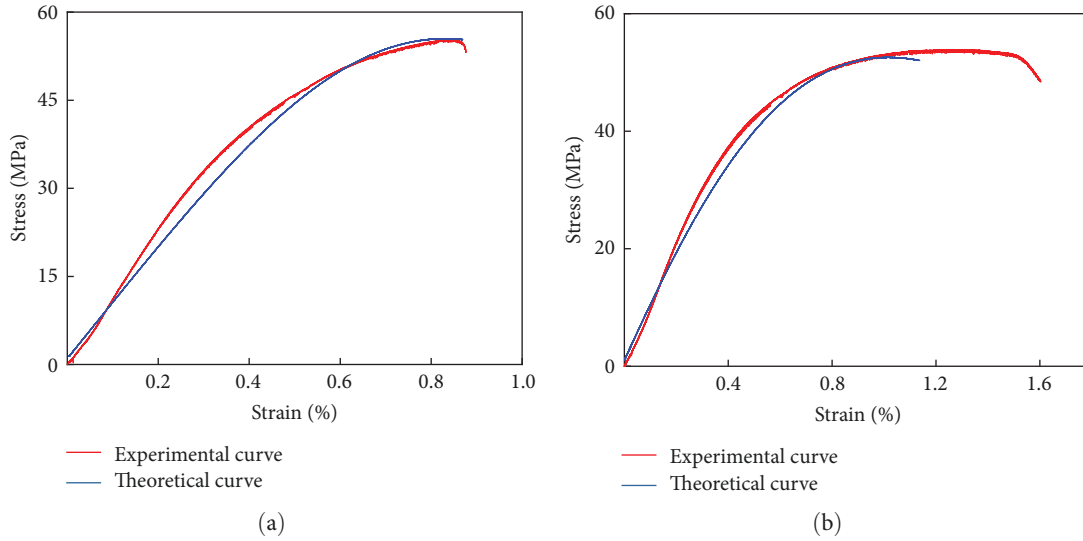


FIGURE 17: Comparison of experimental and theoretical results under the triaxial compression test: (a) two-layer rock-like with interface orientation of 45°; (b) three-layer rock-like with interface orientation of 45°.

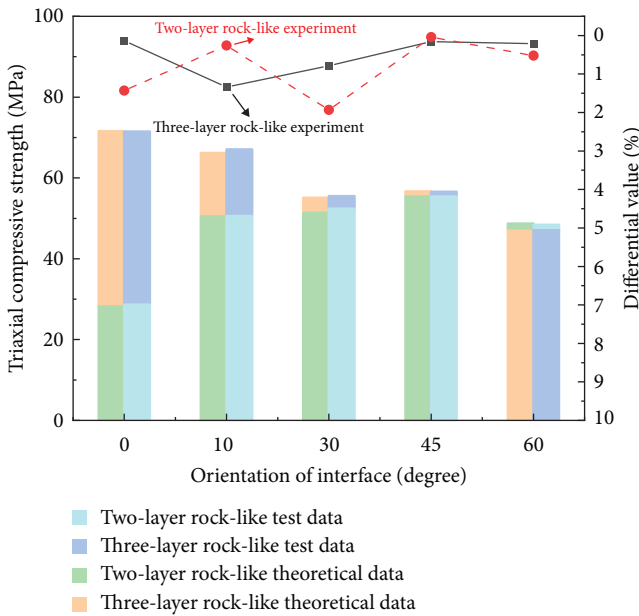


FIGURE 18: Difference between theoretical and experimental values of triaxial compressive strength.

constitutive model could not sufficiently characterize the post-peak stage.

7.4. Model Verification under Triaxial Compression Test. The model parameter  $m$  obtained from Equation (8) is listed in Table 11. The experimental and theoretical curves for the sample with an interface orientation of 45° are shown in Figure 17.

The comparison between the Triaxial test results and the theoretical calculation results is shown in Figure 18.

Because the compaction stage of the specimen in the triaxial compression test was not evident, the proposed

model fitted well with the pre-peak stage of the stress–strain curve of the soft–hard interlocked rock-like samples.

### 8. Conclusions

In this study, the material ratios of similar materials for soft and hard rock-likes were determined using proportioning tests. Soft–hard interlayered rock-like–like samples were prepared, and their porosities were measured using NMR testing to reduce the influence of discreteness on the test results. The following conclusions can be drawn:

- (a) In uniaxial tests, the strength of the combined rock-like specimens exhibited a “U-shaped” distribution as the joint inclination angle varied. At a 45° interface orientation, the strength of the two-layer combined rock-like specimens decreased by 68.75% compared to that at a 0° inclination angle. In contrast, the corresponding three-layer specimens decreased by 25.89%. Compared to the two-layer combined rock-like specimens, the strength of the three-layer combined rock-like specimens increased by 10.53%, 15.63%, 41.67%, 152.02%, and 46.5% as the joint inclination angle increased. Additionally, when the interface angle was 30°, the peak strain of the two-layer rock-like specimens reached its maximum value. In contrast, the peak strain of the three-layer rock-like specimens decreased as the interface angle increased—subsequently, both rock-like specimens transitioned from tensile failure to shear sliding failure.
- (b) In triaxial tests, at the same joint inclination angle, the average strength of the three-layer rock mass increased by 162.23%, 27.16%, 8.57%, 6.49%, and 22.51% compared to the two-layer rock mass. As the joint inclination angle increased, the strength of the two-layer rock mass still exhibited a “U-shaped” distribution, while the strength of the three-layer



rock mass showed a decreasing trend. The peak strain followed a decreasing trend, and the failure mode of the specimen changed from shear dilation or tensile splitting to shear slip. The strength of the three-layer rock-like samples decreased gradually, and the peak strain increased slightly at small interface angles before decreasing gradually. When the interface angle was  $0^\circ$ , the specimens experienced tensile splitting failure, gradually shifting to shear slip failure.

- (c) The damage constitutive model constructed in this study effectively fits the pre-peak stage of the stress-strain curve for the soft-hard interlayered rock-like samples under compression tests. The results of the triaxial compressive strength tests differ from the calculated results of the damage model by 1%–2.5%, while the results of uniaxial compressive strength differ by 0.5%–2.5%. Based on these findings, the damage model developed in this study can reflect the strength and failure behavior of the combined specimens.

## Nomenclature

- $D$ : Damage variable  
 $E$ : Elastic modulus, MPa  
 $m$ : Shape parameter of the Weibull distribution  
 $\nu$ : Poisson  
 $\sigma_f$ : Peak stress, MPa  
 $\sigma_1$ : Major principal stress, MPa  
 $\sigma_3$ : Confining pressure, MPa  
 $\varepsilon_f$ : Peak strain  
 $\varepsilon$ : Major principal strain  
 $\varepsilon_0$ : Strain of the rock microelement.

## Data Availability

The data used to support the findings of this study are available from the corresponding author upon request.

## Conflicts of Interest

The authors declare that there are no conflicts of interest.

## Acknowledgments

This study was supported by the Xi'an Key Laboratory of Geotechnical and Underground Engineering Open Fund Project (XKLGUEKF20-03).

## References

- [1] M. Gao, Z. Liang, S. Jia, Q. Zhang, and J. Zou, "Energy evolution analysis and related failure criterion for layered rocks," *Bulletin of Engineering Geology and the Environment*, vol. 82, no. 12, Article ID 439, 2023.
- [2] B. Pan, W. Yu, and W. Shen, "Experimental study on energy evolution and failure characteristics of rock-coal-rock

- combination with different height ratios," *Geotechnical and Geological Engineering*, vol. 39, no. 1, pp. 425–435, 2021.
- [3] Q. Xie, H. Gao, Y. Ban et al., "Influence of layer thickness ratio on the mechanical and failure properties of soft-hard interbedded rock-like material," *KSCE Journal of Civil Engineering*, vol. 27, no. 11, pp. 4962–4977, 2023.
- [4] S.-Q. Yang, P.-F. Yin, Y.-H. Huang, and J.-L. Cheng, "Deformability and X-Ray micro-CT observations of transversely isotropic composite rock under different confining pressures," *Engineering Fracture Mechanics*, vol. 214, pp. 1–20, 2019.
- [5] M. Noori, G. Khanlari, V. Sarfarazi et al., "An experimental and numerical study of layered sandstone's anisotropic behaviour under compressive and tensile stress conditions," *Rock Mechanics and Rock Engineering*, vol. 57, no. 2, pp. 1451–1470, 2024.
- [6] L. B. Song, G. Wang, X. K. Wang et al., "Failure and acoustic emission characteristics of jointed rock masses with different joint inclination angles and combination mode," *International Journal of Geomechanics*, vol. 22, no. 4, pp. 22–31, 2022.
- [7] Q. Zhang, X. Tang, Y. Zhou, and D. Ma, "Failure and acoustic emission characteristics of interfacial rock masses with different interface inclination angles and combination mode," *Geotechnical and Geological Engineering*, vol. 39, no. 8, pp. 5971–5981, 2021.
- [8] X. K. Chang, S. C. Wu, H. Y. Chen, and X. Fu, "Full-waveform characteristics and frequency spectrum of acoustic emission for fine sandstone," *Journal of Changjiang River Scientific Research Institute*, pp. 118–125, 2022.
- [9] X. Gu, W. Guo, C. Zhang, X. Zhang, C. Guo, and C. Wang, "Effect of interfacial angle on the mechanical behaviour and acoustic emission characteristics of coal-rock composite specimens," *Journal of Materials Research and Technology*, vol. 21, pp. 1933–1943, 2022.
- [10] W. Wang, Y. Ye, Q. Wang, and N. Hu, "Experimental study on anisotropy of strength, deformation and damage evolution of contact zone composite rock with DIC and AE techniques," *Rock Mechanics and Rock Engineering*, vol. 55, no. 2, pp. 837–853, 2022.
- [11] G. Wang, Y. Wang, L. Song et al., "Particle flow simulation of the strength and failure characteristics of a layered composite rock-like sample with a single hole," *Symmetry*, vol. 13, no. 7, Article ID 1132, 2021.
- [12] M. Chen, S.-Q. Yang, P. G. Ranjith, and Y.-C. Zhang, "Cracking behavior of rock containing non-persistent interfaces with various interfaces inclinations," *Theoretical and Applied Fracture Mechanics*, vol. 109, Article ID 102701, 2020.
- [13] S. G. Lekhnitskii and S. Francisco, "Theory of elasticity of an anisotropic elastic body," *Physics Today*, vol. 17, no. 1, Article ID 84, 1964.
- [14] H. Saroglou and G. Tsiambaos, "A modified Hoek-Brown failure criterion for anisotropic intact rock," *International Journal of Rock Mechanics and Mining Sciences*, vol. 45, no. 2, pp. 223–234, 2008.
- [15] Y. M. Tien and M. C. Kuo, "A failure criterion for transversely isotropic rocks," *International Journal of Rock Mechanics and Mining Sciences*, vol. 38, pp. 299–412, 2001.
- [16] F. Gao, R. Guo, W. Wang, Y. Zhang, and S. Zheng, "Investigation of collapse pressure in layered formations based on a continuous anisotropic rock strength criterion," *Geomechanics and Geophysics for Geo-Energy and Geo-Resources*, vol. 9, no. 1, 2023.
- [17] Y. J. Zhang and Y. P. Liu, "Anisotropy of shear strength of layered rocks and determination of shear failure plane," *Rock and Soil Mechanics*, pp. 254–257, 2001.

- [18] S. L. Huang, J. S. Xu, and J. Y. Ma, "Study of layered rock mass composite model based on characteristics of structural plane and its application," *Chinese Journal of Rock Mechanics and Engineering*, pp. 743–756, 2010.
- [19] A. N. Vlasov, V. P. Merzlyakov, and S. B. Ukhov, "Determination of deformation and strength properties of layered rock by asymptotic averaging," *Soil Mechanics and Foundation Engineering*, vol. 40, no. 6, pp. 197–205, 2003.
- [20] P. Luo, D. Li, J. Ma, A. Zhou, and C. Zhang, "Experimental investigation on mechanical properties and deformation mechanism of soft–hard interbedded rock-like material based on digital image correlation," *Journal of Materials Research and Technology*, vol. 24, pp. 1922–1938, 2023.
- [21] P. L. P. Wasantha, P. G. Ranjith, and S. S. Shao, "Energy monitoring and analysis during deformation of bedded-sandstone: use of acoustic emission," *Ultrasonics*, vol. 54, no. 1, pp. 217–226, 2014.
- [22] Y. M. Tien, M. C. Kuo, and C. H. Juang, "An experimental investigation of the failure mechanism of simulated transversely isotropic rocks," *International Journal of Rock Mechanics and Mining Sciences*, vol. 43, no. 8, pp. 1163–1181, 2006.
- [23] J. Huang, Y. Song, M. Lei, C. Shi, C. Jia, and J. Zhang, "Numerical study on the damage characteristics of layered shale using 3D DEM," *KSCE Journal of Civil Engineering*, vol. 27, no. 12, pp. 5436–5447, 2023.
- [24] H. M. Zhang, X. R. Qin, M. Chen, G. S. Yang, and Y. N. Lu, "A damage constitutive model for a jointed rock mass under triaxial compression," *International Journal of Geomechanics*, vol. 23, no. 6, pp. 23–59, 2023.
- [25] Y. Chen, Y. Yang, F. Gao, and X. Zhang, "Researches on damage evolution and acoustic emission characteristics of rocks," *Advances in Civil Engineering*, vol. 2018, Article ID 3108065, 7 pages, 2018.
- [26] T. Ishida, J. F. Labuz, G. Manthei et al., "ISRM suggested method for laboratory acoustic emission monitoring," *Rock Mechanics and Rock Engineering*, vol. 50, no. 3, pp. 665–674, 2017.
- [27] J. Wang, Y. Li, and W. D. Song, "Analysis of damage evolution characteristics of interfacial rock mass with different interface dip angles," *Journal of Harbin Institute of Technology*, vol. 51, pp. 143–150, 2019.
- [28] P. Fu, X. Y. Qi, and S. W. Wang, "Study on damage evolution law of layered composite rock based on acoustic emission experimental," *Science Technology and Engineering*, pp. 9432–8438, 2022.
- [29] L.-J. Ma, X.-Y. Liu, Q. Fang et al., "A new elasto-viscoplastic damage model combined with the generalized hoek-brown failure criterion for bedded rock salt and its application," *Rock Mechanics and Rock Engineering*, vol. 46, no. 1, pp. 53–66, 2013.
- [30] P. Lutz, H. M. Fischer, R. Jenisch et al., "Lehrbuch der Bauphysik," Teubner, Stuttgart, 1985.